The structure of the turbulent boundary layer on a cylinder in axial flow

Richard M. Lueptow[a] and Joseph H. Haritonidis
Massachusetts Institute of Technology, Cambridge, Massachusetts 02139

(Received 6 October 1986; accepted 28 May 1987)

The thick, turbulent boundary layer, which develops as a fluid flows parallel to a cylinder, has been experimentally characterized for the case where the boundary layer is thick compared to the radius of transverse curvature. Measurements of the turbulence intensity, velocity spectra, and intermittency are qualitatively similar to those for the planar boundary layer. Although measurements of wall shear stress using several different techniques have substantial scatter, the wall shear stress appears to be larger than that for the turbulent boundary layer on a flat plate at the same Reynolds number based on streamwise distance. The variable interval time averaging (VITA) and *uv*-quadrant techniques were used to detect the burst cycle near the wall. Conditionally averaged velocities were similar to those for a flat plate boundary layer indicating a similar burst cycle near the wall. However, the VITA frequency scaling indicates an interaction between the flow in the wall region and the outer flow. Flow visualization was used to observe the crossflow of structures in the boundary layer of a cylinder moving through a tank of quiescent water. Large-scale structures were observed moving from the outer region on one side of the cylinder to the outer region on the opposite side of the cylinder suggesting that the wall may be less important in controlling the size and motion of coherent structures in the cylindrical boundary layer than in the planar boundary layer.

I. INTRODUCTION

The structure of turbulence in wall-bounded flows for a flat plate, a channel, and a pipe has been studied extensively. However, the structure of turbulence in the boundary layer on a cylinder, another flow field of simple geometry, has been largely neglected. The analysis of the boundary layer on a cylinder is complicated by the additional length scale related to the transverse curvature of the wall and the fact that the boundary layer thickness δ can grow to be much larger than the radius of the cylinder a.

Several serious attempts have been made toward a detailed experimental study of the properties of the turbulent boundary layer on a cylinder. Most of the previous research has been related to the mean velocity profile.[1–5] Out of these experimental studies, as well as analytical studies based on mixing length or eddy viscosity closures, several proposals for similarity laws have been suggested. These proposals are outlined by Afzal and Narasimha[6] and Lueptow *et al.*[5] Few measurements of the fluctuating velocities in the boundary layer on a cylinder have been made except for measurements of the turbulence intensity and Reynolds stress.[4,5,7]

Aside from the measurements of the mean velocity profile, the turbulence intensity, and the Reynolds stress, no results leading to an understanding of the structure of the turbulence in the boundary layer on a cylinder have been published. The purpose of this paper is to report on measurements and flow visualization results aimed specifically at understanding the structure of turbulence in a cylindrical boundary layer.

[a] Present address: Haemonetics Corporation, Braintree, Massachusetts 02184.

II. EXPERIMENTAL FACILITIES AND PROCEDURE

The experiments described here were carried out in the Acoustics and Vibration Laboratory wind tunnel at the Massachusetts Institute of Technology. This open-circuit wind tunnel is shown in Fig. 1. It has a flow-straightening honeycomb at the inlet and a 20:1 contraction into the 38 cm square test section. Experiments were performed at free-stream velocities U_∞ between 10 and 40 m/sec. The level of free-stream turbulence in the wind tunnel was between 0.1% and 0.3% at these velocities.

Details of the setup of the cylindrical model in the wind tunnel are given by Lueptow *et al.*[5] The cylindrical model was made from a 0.475 cm (0.187 in.) o.d. stainless steel tube suspended along the center line of the wind tunnel. To prevent excessive sag of the cylinder, the cylinder was mounted in 1950 N (440 lb) tension. It was anchored at the downstream end of the test setion to a support attached to the wind tunnel superstructure. The cylinder passed upstream along the tunnel axis and out through the honeycomb at the wind tunnel inlet. A cable attached to the cylinder passed over a pulley and was attached to a lever-arm tensioning device. The cylinder sagged about 3 mm over its 8 m length. A 0.16 cm (1/16 in.) diam O ring around the cylinder at the upstream end of the test section was used to trip the boundary layer. Table I shows the characteristics of the boundary layer at the measurement location. [The + subscript denotes nondimensionalization using inner scales, ν (kinematic viscosity), and U_τ (friction velocity).]

Mean and fluctuating velocities were measured using U and X probes that were mounted at the tip of an airfoil sting that could be traversed along the length of the wind tunnel test section. The hot-wire probes were made from jeweler's broaches ground to 0.025 mm (0.001 in.) diam that were

 0031-9171/87/102993-13$01.90 © 1987 American Institute of Physics

Downloaded 02 Oct 2003 to 129.105.69.38. Redistribution subject to AIP license or copyright, see http://ojps.aip.org/phf/phfcr.jsp

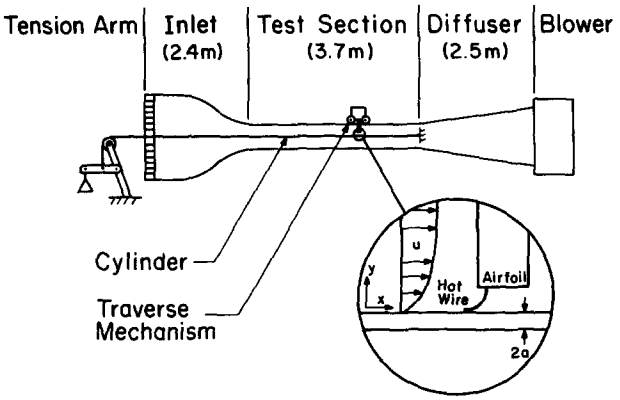

FIG. 1. Sketch of wind tunnel showing tensioning device, cylinder, and hot-wire traverse mechanism.

soldered to lead wires and epoxied into the holes of a small diameter ceramic thermocouple insulator. The sensing wire was 1.25 μm Pt–Rh (90/10) alloy. The U probe had a sensing length of 0.25 mm (0.010 in.). The nondimensional sensing lengths l_+ are shown in Table I. The X probe had a box size of 0.5 mm (0.020 in.). The hot-wire probes were used in conjunction with Disa 55D05 constant temperature anemometers. The hot-wire probes had a cold resistance higher than the standard commercially available probes. Since the anemometers were designed to be used with commercially available probes, the response of the anemometer/hot-wire system to a standard square wave test was slightly underdamped. This did not appear to cause any error in the measured velocities.

A Hewlett Packard 2250 measurement and control unit, modified with an external sample and hold circuit to allow simultaneous sampling on four channels, was used to sample the anemometer output. The nondimensional time between samples Δt_+ is shown in Table I. The digitized data were stored and processed on a Hewlett Packard 1000-A900 computer.

The X probe calibration scheme was based on directly measuring the voltage output of the X probe at different combinations of U and V velocities. To expose the X probe to different velocity components, the probe was situated at five to seven different angles with respect to the mean flow in the wind tunnel. The voltage from each wire of the probe was measured at four to six different velocities for each angle. The velocity components, determined from the free-stream velocity and the angle of the X probe with respect to the free stream, and the corresponding anemometer outputs were used to generate a calibration table. This method is similar to that used by Willmarth and Bogar[8] for X-probe calibration.

TABLE I. Characteristics of flow and measurement at 1.4 m downstream of the trip.

Nominal U_∞ (m/sec)	10	20	40
$\delta_{0.99}$ (cm)	1.9	1.7	1.6
Re_θ	2.0×10^3	3.3×10^3	5.6×10^3
U_τ/U_∞ (sublayer probe)	0.0450	0.0435	0.0419
l_+	7.7	14.8	28.6
Δt_+	0.66	1.31	4.40
Sampling freq. (kHz)	22	44	44

III. MEASUREMENTS

A. Turbulence intensity

Measurements of the streamwise turbulence intensity $u_{\rm rms} = \sqrt{\overline{u'^2}}$ were made using a U probe. (Here u' is the fluctuation in the streamwise velocity U such that $U = \overline{U} + u'$, where $\overline{U}$ is the mean velocity.) The turbulence intensity of the velocity perpendicular to the wall, $v_{\rm rms} = \sqrt{\overline{v'^2}}$, is based on X-probe measurements. The streamwise velocity fluctuations were corrected for the length of the hot-wire probe to avoid errors in the magnitude of $u_{\rm rms}$ caused the averaging of fluctuations over the length of the hot wire. Willmarth and Sharma[9] found that for a hot-wire length as small as $l_+ \sim 10$, about 8% of the rms velocity fluctuations could not be resolved at a distance from the wall of $y_+ \sim 13$. To correct for this error an empirical correction factor was estimated based on data compiled by Johansson and Alfredsson[10] for the maximum rms velocity fluctuation as a function of l_+. The correction factor was set equal to 1.0 for $l_+ \sim 10$, increasing linearly with l_+. The maximum correction factor for the hot-wire lengths shown in Table I is 1.06 at 40 m/sec. The correction factor was applied to the measured values of $u_{\rm rms}$ at all distances from the wall, even though the correction is based on the maximum rms velocity. No corrections were applied to the X-probe measurements.

The turbulence intensity is shown in Fig. 2. The maximum amplitude of the corrected $u_{\rm rms}$ is about 3.2 times the friction velocity U_τ, determined from shear probe measurements described later. This is slightly higher than the usual values for the maximum $u_{\rm rms}$ normalized with the friction velocity for a planar boundary layer[9] and channel flow.[10] The difference may be a consequence of the difficulty in measuring the friction velocity, as discussed later in this section. The maximum $u_{\rm rms}$ for all velocities occurs at a distance from the wall of $y_+ \sim 13$. This is approximately the same

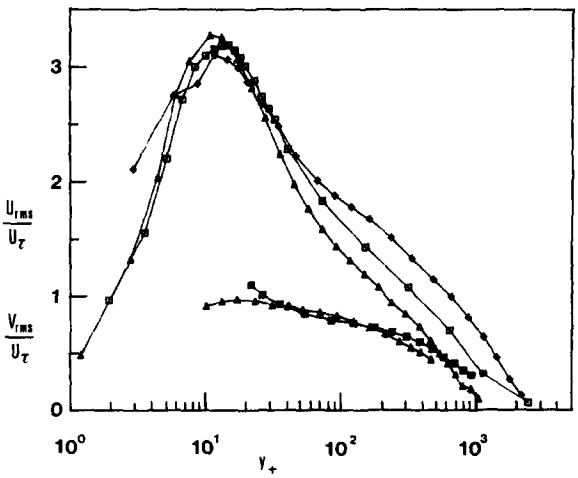

FIG. 2. Profile of streamwise turbulence intensity (open symbols) and turbulence intensity perpendicular to the wall (filled symbols) 1.4 m downstream of the trip. Here △ $U_\infty = 10.5$ m/sec; □ $U_\infty = 21.9$ m/sec; ◇ $U_\infty = 41.0$ m/sec; ▲ $U_\infty = 9.9$ m/sec; ■ $U_\infty = 20.4$ m/sec.

Downloaded 02 Oct 2003 to 129.105.69.38. Redistribution subject to AIP license or copyright, see http://ojps.aip.org/phf/phfcr.jsp

location as for a planar boundary layer[9] and a channel flow.[10]

The measurements of v_{rms} were severely limited by the spatial resolution of the X probe. But the measurements using an X probe were confirmed by comparison to those obtained with a U probe for u_{rms}. The X-probe measurements of u_{rms} were low by about 10% as compared to the U-probe measurements, except near the wall where the difference was greater. The difference was most likely caused by the poor spatial resolution of the X probe. The maximum value of v_{rms}/U_τ was measured to be 1. This value is the same as that for the planar boundary layer[11] and channel flow.[12]

The similarity in the magnitude of the maximum turbulence intensity and its distance from the wall between the cylindrical boundary layer and other wall-bounded flows suggest that the mechanism for the generation of turbulence is the same, at least in the wall region.

B. Velocity spectra

The streamwise velocity spectra presented in this section were obtained using a U probe, and the spectra for the velocity perpendicular to the wall were based on X-probe measurements. In both cases, the U-probe voltages were low-pass filtered at the Nyquist frequency to prevent aliasing. No corrections were made for the hot-wire length. The energy density E is nondimensionalized so that the total turbulent energy, or the area under each curve, is equal to unity.

The frequency f can be nondimensionalized with either an outer time scale, $f_0 = f\delta/U_\infty$, or an inner time scale, $f_+ = fv/U_\tau^2$. Figure 3 compares these two nondimensionalization schemes for different Reynolds numbers. The outer scaling for the frequency appears to provide somewhat better collapse than the inner scaling, especially at low frequencies. Inner scaling provides the best collapse of the data for spectral measurements made very close to the wall ($y_+ < 10$, not shown in Fig. 3).

The streamwise velocity spectra for various locations in the boundary layer are shown in Fig. 4 for a free-stream velocity of 10.5 m/sec. The individual curves all have the same overall shape. (The large peak in the spectrum in Fig. 4 for $y_+ \sim 399$ corresponds to 155 Hz. The peak may be an anomaly, but this cannot be shown conclusively.) The maximum turbulent energy occurs in the same frequency band regardless of the distance from the wall. The smallest contributions of high frequencies occur very near the wall and in the outer part of the boundary layer. The small contribution of high frequencies in the outer part of the boundary layer is not surprising, since large scales (low frequencies) would be expected to dominate.

The results shown in Fig. 4 lend credence to the constant eddy viscosity arguments put forth by Lueptow *et al.*[5] They postulated that the cylinder is so small compared to the size of the eddies that the wall cannot constrain the size of the eddies, as it does in the planar boundary layer. Since the spectra in Fig. 4 are so similar, there is little difference in the size distribution of eddies for different points in the boundary layer. Thus the wall is likely to play a minimal role in constraining the size of eddies, and the constant eddy viscosity assumption may be appropriate.

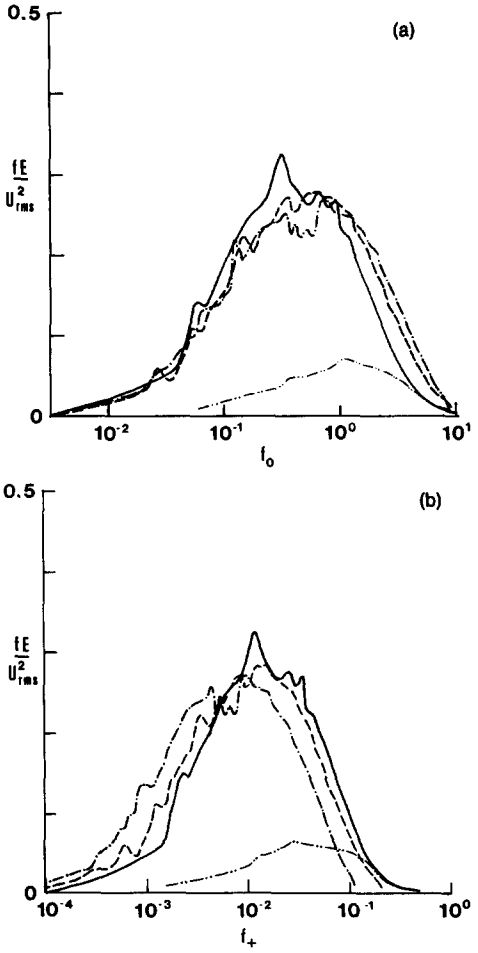

FIG. 3. Streamwise velocity spectra: — $U_\infty = 10.5$ m/sec, $y_+ \sim 37$; --- $U_\infty = 21.9$ m/sec, $y_+ \sim 32$; -·-·- $U_\infty = 41.0$ m/sec, $y_+ \sim 47$. Spectrum of velocity perpendicular to the wall: -··-··-·· $U_\infty = 9.9$ m/sec, $y_+ \sim 37$. (a) Outer scaling. (b) Inner scaling. Measurements at 1.4 m downstream of trip.

The spectrum for the velocity fluctuations perpendicular to the wall is shown in Fig. 3. The smaller amplitude of the velocity fluctuations perpendicular to the wall is reflected in the v spectrum. The maximum energy in the v fluctuations occurs at a higher frequency than that for the u fluctu-

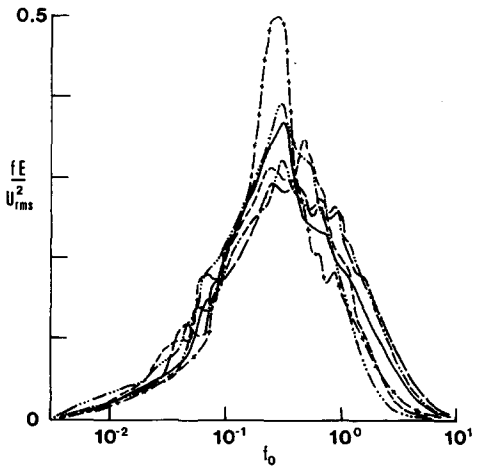

FIG. 4. Streamwise velocity spectra at $U_\infty = 10.5$ m/sec (outer scaling): -···-···-··· $y_+ \sim 2$, --- $y_+ \sim 13$, -··-··-·· $y_+ \sim 37$, ––– $y_+ \sim 78$, — $y_+ \sim 158$, -+-+-+ $y_+ \sim 399$. Measurements were made 1.4 m downstream of trip.

Downloaded 02 Oct 2003 to 129.105.69.38. Redistribution subject to AIP license or copyright, see http://ojps.aip.org/phf/phfcr.jsp

ations. At higher frequencies the two spectra merge. Lawn[13] found the same results for pipe flow.

C. Intermittency

Many detection schemes have been used to discriminate turbulent from nonturbulent flow to determine the intermittency at the edge of the boundary layer.[14] The detection function D in (1) was chosen since it detects sharp changes in the velocity usually associated with turbulence. Here $D(t,T)$ is based on a moving average of the square of the time derivative of the velocity signal, where T is the averaging time. The square of the time derivative is used to enhance the detection function's sensitivity to sharp fluctuations in velocity:

$$D(t,T) = \int_{t-T/2}^{t+T/2} \left(\frac{du'}{dt}\right)^2 dt. \tag{1}$$

When the detection function D exceeds a criterion level k the flow is said to be turbulent. The intermittency γ is simply the fraction of the total time for which the flow is turbulent.

Although the procedure for detection of turbulence is straightforward, the intermittency is dependent on k and T. To avoid the arbitrary selection of an averaging time T, it was assumed that the averaging time is approximately equal to the outer time scale ($T = t_0 = \delta/U_\infty$). Changes in T of $\pm 50\%$ resulted in a change of only $\pm 7\%$ at any given k. The trigger level k was adjusted so that $D \geqslant k$ for turbulent periods by observing the magnitude of the detection function corresponding to a velocity record for which distinct periods of turbulent and nonturbulent flow were observable. After the initial selection of the trigger level k, other velocity records were evaluated using the same k and T. In each case, the detected periods were checked against the velocity record for accuracy in detecting periods of turbulence.

The intermittency is shown in Fig. 5. The data for all three Reynolds numbers collapse onto a single curve. The curve through the data is based on the assumption that the probability density function of the instantaneous interface position η is nearly Gaussian.[15] Given the Gaussian distribution, the intermittency $\gamma(y)$ takes the form of the error function,

$$\gamma(y) = 0.5\{1 - \text{erf}\,[(\eta - \eta_1)/\sqrt{2}\sigma]\}_{y=\eta}. \tag{2}$$

Here η_1 is the average position of the interface and σ is the standard deviation of the position of the interface. Using the data in Fig. 5, $\eta_1/\delta = 1.0$ compared to an average position of the interface of about 0.8 in a planar boundary layer. The standard deviation σ was adjusted until the curve defined by (2) fit the data. The best fit was obtained for $\sigma/\delta = \sigma/\eta_1 = 0.18$.

The difference in the average position of the interface between the cylindrical boundary layer and the planar boundary layer[16] is substantial. While no conclusive statement can be made about this difference, two explanations are plausible. First, u'/U_∞ is about 20% larger in the axisymmetric boundary layer than in the planar boundary layer for $y/\delta_{0.99} > 0.8$. Since the velocity fluctuations in the axisymmetric boundary layer are more energetic in the outermost part of the boundary layer, the turbulent eddies probably have a longer life and distribute their energy over a larger region before being dissipated, thus raising the intermittency level. Second, since the cylinder does not constrain the motion of eddies like a wall does, these eddies can easily move across the axisymmetric boundary layer "filling out" the boundary layer with turbulent eddies. As a result, the intermittency level is nearly one out to $y/\delta \sim 0.7$ compared to the $y/\delta \sim 0.4$ in the planar case.

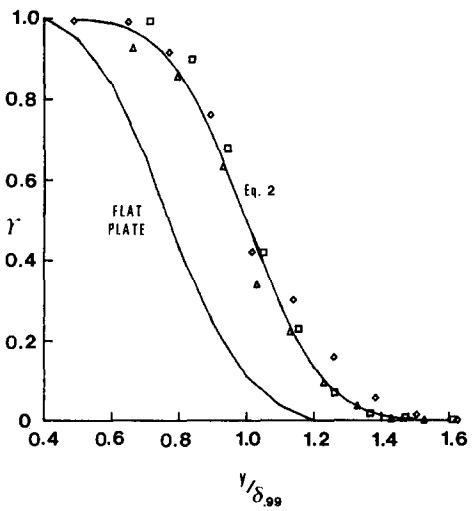

FIG. 5. Intermittency γ determined from the detection function. Intermittency determined from detection function for a flat plate is from Ref. 16 ($Re_\theta \sim 3000$). Here △ $Re_\theta \sim 2000$ (10.2 m/sec), □ $Re_\theta \sim 3300$ (20.3 m/sec), ◇ $Re_\theta \sim 5300$ (37.5 m/sec). Measurements were made 1.4 m downstream of trip.

D. Wall shear stress

Since the relationship between the mean velocity profile and the wall shear stress, τ_w, in the turbulent boundary layer on a cylinder is not known, most common methods of measuring the wall shear stress, such as through the use of a Preston tube, are not appropriate. However, measurements of the mean wall shear stress on the cylinder have been accomplished using an instrument similar to a Preston tube except that the opening of the device lies within the viscous sublayer. The sublayer wall shear stress probe consists of a thin piece of brass with a shallow channel (1.0 mm wide by 0.1 mm deep) leading to a pressure tap as described by Fulcher.[17] The probe is mounted on the surface on which the wall shear stress is to be measured with the channel against the surface and the opening of the channel facing upstream. In this way the resultant pressure can be measured within the viscous sublayer.

A flat sublayer probe was calibrated in a planar boundary layer against a Preston tube.[17] Measurements were made in the cylindrical boundary layer with a geometrically similar curved sublayer probe using the calibration obtained from the flat plate measurements. The planar calibration could be used in the cylindrical boundary layer because of the small difference (about 2% in this case) between the sublayer law in the cylindrical boundary layer[18] and the planar sublayer law.

The coefficient of friction $C_f = 2\tau_w/\rho U_\infty^2$ measured using the sublayer probe and several other techniques is shown

Downloaded 02 Oct 2003 to 129.105.69.38. Redistribution subject to AIP license or copyright, see http://ojps.aip.org/phf/phfcr.jsp

in Fig. 6. The coefficients of friction for three different velocities are plotted as a function of the Reynolds number based on distance along the cylinder, Re_x. Of course, since the boundary layer was tripped, the distance along the cylinder was difficult to determine. To determine an approximate Re_x, it was assumed that the boundary layer structure at a given location downstream of the trip is the same as if the boundary layer had developed naturally from a leading edge and a trip were not used. Two further assumptions were necessary. First, a linear relation exists between the distance from the virtual leading edge to the trip and the free-stream velocity. Second, the momentum thickness Reynolds number Re_θ is a function of Re_x. Although calculating the momentum thickness from experimental data is subject to some error, the axisymmetric definition for the momentum thickness[19] was used to estimate Re_θ at several Re_x. A simple linear relation between the distance from the virtual leading edge to the trip and the free-stream velocity was estimated by minimizing the correlation coefficient between Re_θ and Re_x. This linear relation was used to calculate a corrected Re_x for use in Fig. 6.

Three curves are included in Fig. 6. The lower curve is the empirical relation for the coefficient of friction in the planar boundary layer.[20] The upper curve is the predicted relationship between the coefficient of friction and the Reynolds number extracted from Fig. 2 of White[21] (verified by Ackroyd[22]) for a Reynolds number based on the cylinder radius of $Re_a = 3200$ (corresponding to $U_\infty = 20$ m/sec for the cylinder used in this study). The middle curve is a linear regression fit to the sublayer probe data given by $C_f = 0.0123\ Re_x^{-0.08}$. The deviation of the wall shear stress from the mean of the wall shear stress measured at four different circumferential locations was less than 5%. Willmarth *et al.*[3] found variation of the order of 10% for Preston tube measurements on cylinders with $\delta/a \leqslant 4$.

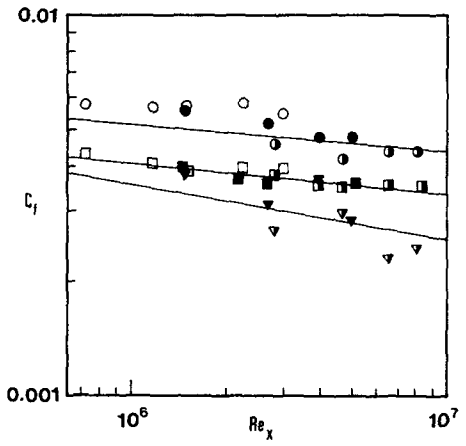

FIG. 6. Coefficient of friction measured on the top of the cylinder. Symbols correspond to different methods of estimating the coefficient of friction: ○ matching sublayer profile to planar law of the wall, □ sublayer probe, ▽ slope of Reynolds stress versus a/r. Open symbols correspond to 12.5 m/sec, filled symbols correspond to 20 m/sec, half-filled symbols correspond to 30 m/sec. The middle curve is based on a regression fit to the data for the sublayer probe. The lower curve is an empirical relation for a flat plate.[20] The upper curve is the predicted relation for a cylinder[21] for $Re_a = 3200$ (corresponding to 20 m/sec).

For all three velocities shown, the coefficient of friction is higher than that for a planar boundary layer. This agrees with the prediction of Eckert,[23] Cebeci,[24] White,[21] and White, Lessmann, and Christoph.[25] White's predicted coefficient of friction (upper curve in Fig. 6) is higher than that measured, but, considering the assumptions necessary in his analysis, the agreement is reasonable.

Willmarth *et al.*[3] described a method of indirectly determining the wall shear stress by fitting the mean velocity data to the inner and buffer zone of the planar wall of the wall, as tabulated by Coles,[26] by adjusting the friction velocity. Results using this method are included in Fig. 6. The coefficients of friction determined in this way are much larger than the values obtained from the shear stress probe or predicted by White,[21] especially at lower Reynolds numbers. This may be a result of artificially high velocities measured near the wall because of heat transfer between the hot wire and the cylinder.

Another method of determining the wall shear stress, based on the constant shear moment relation in the cylindrical boundary layer, is to determine the slope of the Reynolds stress plotted versus a/r. The results presented by Lueptow *et al.*[5] using this method are included in Fig. 6. The errors in the coefficient of friction calculated using this method are substantial for several reasons. First, the method is dependent on determining the slope of measured data, which is inherently difficult. Second, the measurements of the Reynolds stress used for this analysis were made with a commercially available TSI X probe with poor spatial resolution.

All of the above methods of determining the coefficient of friction have their limitations as noted. However, the coefficients of friction calculated using the different methods all show the same trends. First, the coefficient of friction measured in a cylindrical boundary layer is higher than that for a planar boundary layer at the same Reynolds number. Second, the coefficient of friction for a cylindrical boundary layer tends to decrease with Reynolds number, although perhaps not as quickly as the coefficient of friction for a planar boundary layer.

Kennedy, Bakewell, and Zimmermann[27] made measurements of the coefficient of friction by towing small cylinders in a tow tank. Their results have considerable scatter, which was most likely caused by the wake of the tow body interfering with the cylindrical boundary layer. However, the results described in this section fall within the range of values found by Kennedy *et al.* at the appropriate Reynolds number based on cylinder radius.

The data shown in Fig. 6 suggest a slight dependence of C_f on the free-stream velocity for a given Re_x. This could be a result of poor estimates of Re_x because of the boundary layer trip. On the other hand, this may suggest dependence of the coefficient of friction on another parameter of the flow. Kennedy *et al.* suggest that C_f depends on both Re_x and the ratio of the length of the cylinder to its diameter.

The coefficient of friction obtained using the shear stress probe seems to provide the most consistent results with the greatest precision. Therefore results requiring the estimation of the friction velocity for nondimensionalization are based on the shear stress probe measurements.

Downloaded 02 Oct 2003 to 129.105.69.38. Redistribution subject to AIP license or copyright, see http://ojps.aip.org/phf/phfcr.jsp

IV. STRUCTURE OF TURBULENCE

A. Flow visualization

Flow visualization was used to observe the motion of large-scale structures in the turbulent flow field of a cylinder moving through a tank of quiescent water as shown in Fig. 7. Unlike a boundary layer, streamwise gradients in this flow field are essentially zero. However,the local mechanism for the generation of turbulence is expected to be the same in both cases.

The cylinder was made from a long 0.318 cm (0.125 in.) diam Buna-N cord, or O ring, cemented end-to-end to form a loop. The O ring was mounted on four pulleys, and one of the upper pulleys was driven by a dc motor. The lower two pulleys were submerged in the water tank, so that the O ring moved through the water and a boundary layer developed on its surface. The stationary idlers, positioned near the lower pulleys, were necessary to minimize oscillations of the cylinder excited by the pulleys. The distance between the upstream false wall and the downstream stationary idler was 80 cm ("downstream" is in the direction of the motion of the cylinder). The flow was observed at a point between 55 and 65 cm downstream from the false wall. The "hydrogen bubble method" was used to visualize the flow. Since oxygen bubbles are larger and more easily observed than hydrogen bubbles, they were used instead of hydrogen bubbles. A small platinum wire was positioned at the "point of observation," slightly above the cylinder and perpendicular to it. In this position the bubbles would slowly rise vertically above the cylinder unless entrained in the boundary layer of the moving cylinder. A Video Logic, Inc., Instar model IV video system with strobes matched to the video rate of 120 frames/sec was used to record the flow. The strobes illuminated a 2 cm thick plane of the flow. Still photos of the video display are shown here.

Figure 8 shows a sequence of events as the turbulence carries a line of bubbles formed at the platinum wire at a height $h = 1$ cm above the cylinder. Most bubbles are carried along in the boundary layer and eventually rise into the quiescent fluid. At times, though, the bubbles are carried to the opposite side of the cylinder as shown in Figs. 8(b)–8(d). The details of this event vary and are usually not as distinct as shown in the photos. Bubbles starting above the cylinder near the wall end up below the cylinder in the outer part of the boundary layer following an arclike path. As the bubbles move along the arc, the group of bubbles elongates along the arc. The arclike path is circumferential indicating a w (azimuthal) component of velocity associated with the large-scale structures in the boundary layer.

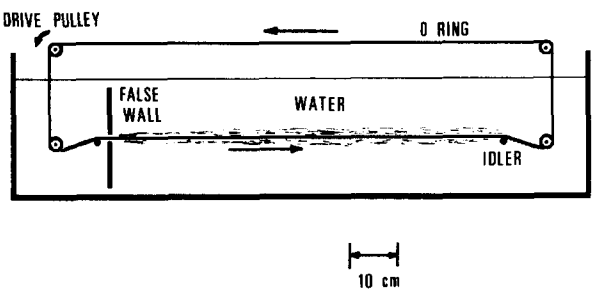

FIG. 7. Sketch of tank and O ring setup used for flow visualization.

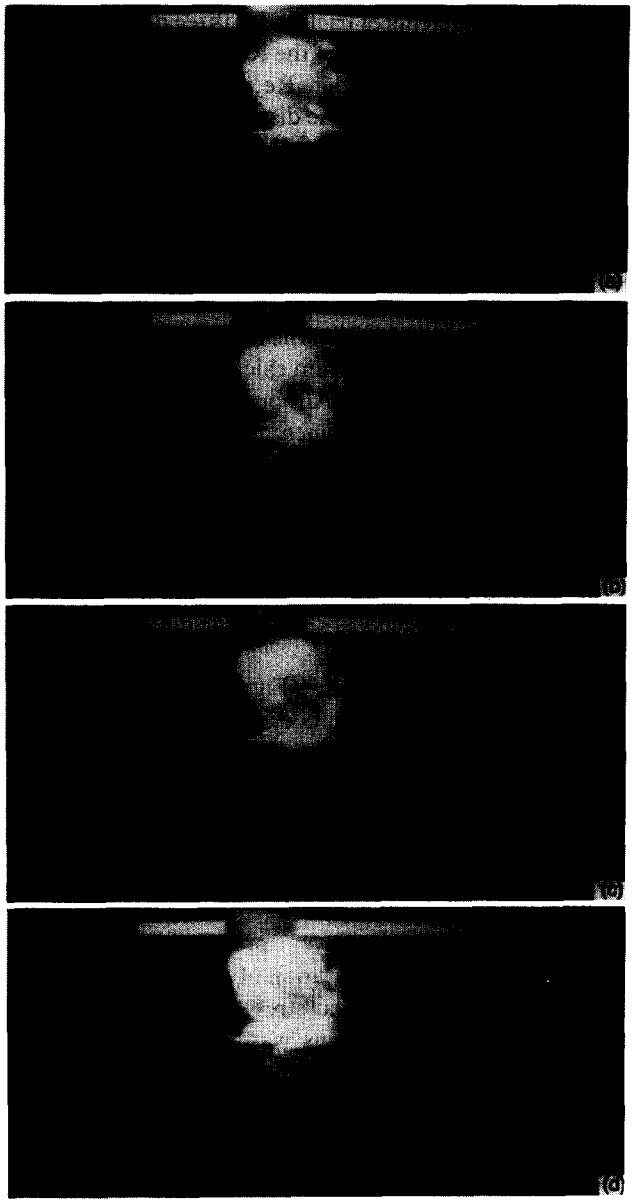

FIG. 8. Oblique view of flow visualization using bubbles ($h/\delta \sim 0.26$, $\mathrm{Re}_x \sim 5\times 10^6$, $\mathrm{Re}_a = 550$, $a_+ \sim 26$). The time between photographs is 0.5 sec. (a) Bubbles move downward toward the cylinder (arrow shows the direction of cylinder motion). (b) Bubbles begin to pass under the cylinder. (c) Bubbles are carried further below the cylinder and downstream. (d) Bubbles are carried further downstream and are dispersing making further visualization difficult.

These events occur intermittently, and their frequency decreases with increasing height of the bubble wire above the cylinder. For the closest position of the bubble wire to the cylinder, $h/\delta \sim 0.1$ ($h = 0.4$ cm), groups of bubbles passed below the cylinder at a rate of $f_0 \sim 0.05$. This is slightly less than the VITA burst frequency measured for negative events (see Sec. IV B and Fig. 9).

The flow visualization suggests that the turbulent transport of fluid in the boundary layer on the cylinder is very different from that in the planar boundary layer. This is because the flow is less constrained by the wall in the boundary layer on a cylinder than in the boundary layer on a flat plate

Downloaded 02 Oct 2003 to 129.105.69.38. Redistribution subject to AIP license or copyright, see http://ojps.aip.org/phf/phfcr.jsp

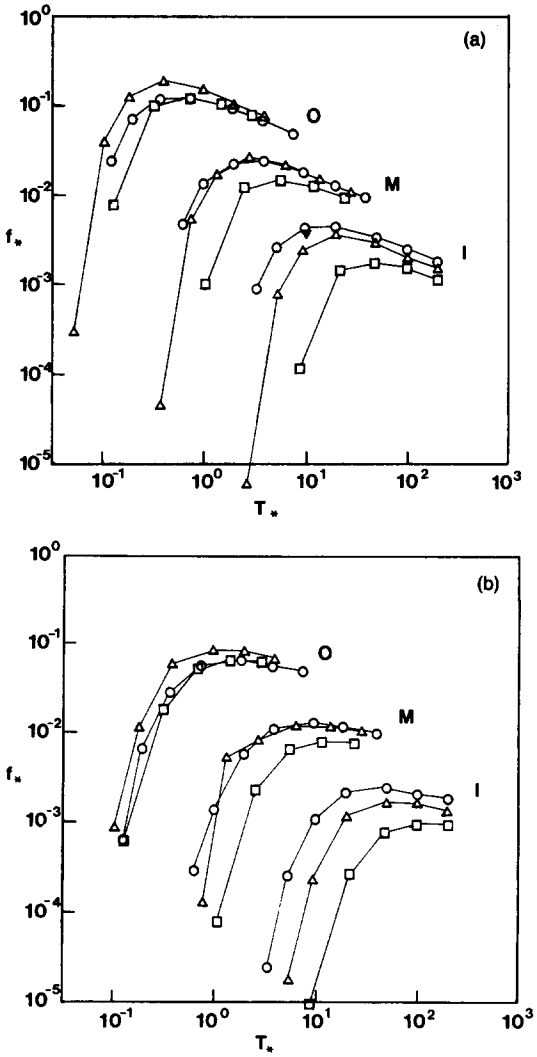

FIG. 9. Scaling of corrected VITA burst frequency f_* as a function of averaging time T_* for $k = 1.0$. Inner time scale (I) is $t_+ = \nu/U\tau^2$, outer time scale (O) is $t_0 = \delta/U_\infty$, mixed time scale (M) is $t_m = (t_+ t_0)^{1/2}$. Here ○ $U_\infty = 10.5$ m/sec, $y_+ \sim 37$; △ $U_\infty = 20.7$ m/sec, $y_+ \sim 33$; □ $U_\infty = 41.0$ m/sec, $y_+ \sim 47$; ▼ planar data[30] (inner scaling, $y_+ \sim 15$, $\mathrm{Re}_\theta \sim 3000$). (a) Accelerating events. (b) Decelerating events.

resulting in a significant w component of velocity. Thus fluid can be transported from one side of the cylinder to the opposite side by these large-scale, cross-flow structures.

B. VITA event detection

Variable interval time averaging,[28] or VITA, is based on the detection of layers of high shear that are associated with turbulence production by the burst cycle described in detail by Kline *et al.*[29] The burst cycle is believed to be responsible for generating most of the turbulent velocity fluctuations in the boundary layer. The VITA method depends on the detection of peaks in the short-time variance of the streamwise velocity signal. Positive, or accelerating, VITA events occur when $du'/dt > 0$ and indicate a streamwise acceleration of the fluid. Negative, or decelerating, VITA events occur when $du'/dt < 0$ and indicate a streamwise deceleration of the fluid.

Positive VITA events can be correlated to the burst cycle in the following way. Before the VITA event is detected, the velocity at the probe decreases as the low-speed fluid from near the wall lifts up and passes the probe. Then the velocity at the probe increases sharply as high-speed fluid sweeps in toward the wall. This sharp acceleration results in a large short-time variance and is detected by VITA. The velocity reaches a local maximum as the sweep proceeds. Then the velocity decreases to its mean as the effect of the burst cycle subsides. Negative VITA events are more difficult to interpret.

The drawback of the VITA event detection technique is that the number of the events detected is dependent on the two parameters of the detection scheme, k and T, where T is the averaging time and k is the trigger level for detection. In this case the burst frequency was calculated for several values of k and T, and similarity was determined on the basis of this limited number of values. Ideally, similarity should be determined on the basis of matching surfaces of burst frequencies, at different Reynolds numbers, determined for many combinations of k and T.

The burst frequency is shown in Fig. 9 using inner, outer, and mixed scaling for a U probe positioned at an average $y_+ \sim 39$ ($33 < y_+ < 47$). The nondimensional burst frequency f_* is plotted as a function of the appropriately nondimensionalized VITA averaging time T_* for $k = 1.0$. Similar collapse of the data was obtained using $k = 0.6$ and $k = 1.4$. Figure 9 shows that the poorest collapse of the data for both accelerating events and decelerating events results when using inner scaling. Both the outer scaling and the mixed scaling provide better collapse suggesting that the outer flow has a strong influence on the events at the wall. Blackwelder and Haritonidis[30] found that the burst frequency scales with the inner time scale, $t_+ = \nu/U_\tau^2$, for the boundary layer on a flat plate. Alfredsson and Johansson[31] found that a mixed time scale, $t_m = (t_+ t_0)^{1/2}$, where $t_0 = b/U_\infty$, collapsed the burst frequency data best for a turbulent flow in a channel of height b. The burst frequency for accelerating events is of the same order of magnitude as the burst frequency in the planar boundary layer[30] at similar Reynolds numbers based on the momentum thickness as shown in Fig. 9(a).

The frequency of the large-scale, cross-flow structures determined from the flow visualization can be compared to the frequency of VITA events. Although the Reynolds number based on momentum thickness for the flow visualization is difficult to determine, it is estimated to be between 10^3 and 10^4. This in the same range as the Reynolds numbers for the burst frequency plotted in Fig. 9. The event frequency for $h/\delta \sim 0.1$ ($y_+ \sim 75$) in the flow visualization was $f_0 \sim 0.05$. This is just slightly lower than the burst frequency measured for negative VITA events at $T_* \sim 1$, suggesting a relationship between cross-flow structures seen in the flow visualization and negative VITA events. Care must be taken in this comparison, since the event frequency was measured at a different y_+. A lower event frequency would be expected at the larger distance from the wall. In any case, the events detected using VITA may be related to the cross-flow, large-scale structures observed in the flow visualization.

Figure 10 shows the conditional averages for $k = 1$ and $T_+ = 20$ obtained using an X probe. (The conditional aver-

Downloaded 02 Oct 2003 to 129.105.69.38. Redistribution subject to AIP license or copyright, see http://ojps.aip.org/phf/phfcr.jsp

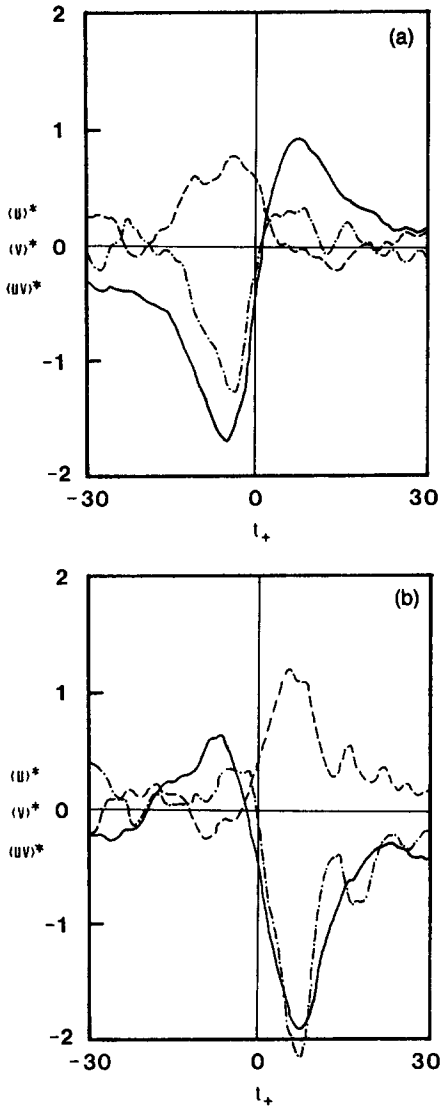

FIG. 10. Conditional averages of events based on VITA detection on streamwise velocity for $k = 1$ and $T_+ = 20$ ($U_\infty = 9.9$ m/sec, $y_+ \sim 39$). Here — $\langle u\rangle^*$, --- $\langle v\rangle^*$, $-\cdot-\cdot-$ $\langle uv\rangle^*$. (a) Accelerating events (103 members). (b) Decelerating events (57 members).

ages for u' obtained using the X probe were consistent with the conditional averages obtained using a U probe with better spatial resolution.) The conditional averages are normalized so that $\langle u\rangle^* = \langle u'\rangle/k^{1/2}u_{\rm rms}$, $\langle v\rangle^* = \langle v'\rangle/k^{1/2}v_{\rm rms}$, and $\langle uv\rangle^* = \langle u'v'\rangle/ku_{\rm rms}v_{\rm rms}$. In the case of accelerating events, Fig. 10(a), the shear layer in the streamwise direction associated with the burst cycle is evident. The largest contribution to the Reynolds stress occurs before the midpoint of the event during the ejection portion of the cycle. The conditional averages for decelerating events are shown in Fig. 10(b). The streamwise velocity increases first and then drops off sharply resulting in detection by VITA. After the sharp drop in streamwise velocity, v' becomes positive, resulting in a large negative Reynolds stress after the midpoint of the event. In both accelerating and decelerating events, the largest Reynolds stress is associated with the liftup of low-speed fluid (negative u' and positive v').

Qualitatively, the conditional averages are similar to those obtained for a turbulent channel flow[12] for slightly different T_+. Based on the conditional average for accelerating VITA events, the low-speed fluid moves away from the wall at an angle of about 7°. The sweep-type motion approached the wall at an angle of about 1°. This compares to 4.6° and 1.6°, respectively, measured for turbulent channel flow[12] with $k = 1$ and $T_+ = 10$. Although the flow angles differ, the similarity in the conditional averages again suggests that the mechanism of the generation of turbulence in the cylindrical boundary layer is similar to that of turbulent channel flow.

C. The *uv*-quadrant event detection

The uv-quadrant detection method of event detection involves sorting pairs of u' and v' into the appropriate quadrant in the u'-v' plane (u' is the abscissa and v' is the ordinate) and using the amplitude of individual realizations of the product $u'v'$ in comparison to a threshold for event detection.[32] It is common to associate quadrant 2 (negative u' and positive v') with the ejection phase of the burst cycle, since low-speed fluid lifts up from the wall. Quadrant 4 (positive u' and negative v') is often associated with the sweep, since high-speed fluid moves toward the wall. High Reynolds stress events can be detected by considering high-energy $u'v'$ pairs where the detection criterion $|u'v'| > Hu_{\rm rms}v_{\rm rms}$ is met.[12]

The fractional contribution to the Reynolds stress by each quadrant is shown in Fig. 11 as a function of H. Quadrants 2 and 4, which are negative $u'v'$ products, make a positive contribution to the Reynolds stress, while quadrants 1 and 3, which are positive $u'v'$ products, make a negative contribution to the Reynolds stress. At $H = 0$, the sum of the contribution by all $u'v'$ pairs to the Reynolds stress is equal to 1. From Fig. 11 it is evident that the ejection, or quadrant 2 $u'v'$ pairs, offer the largest contribution to the Reynolds stress. Even for very large H, quadrant 2 pairs contribute appreciably to the Reynolds stress.

These results are qualitatively similar to the results for a

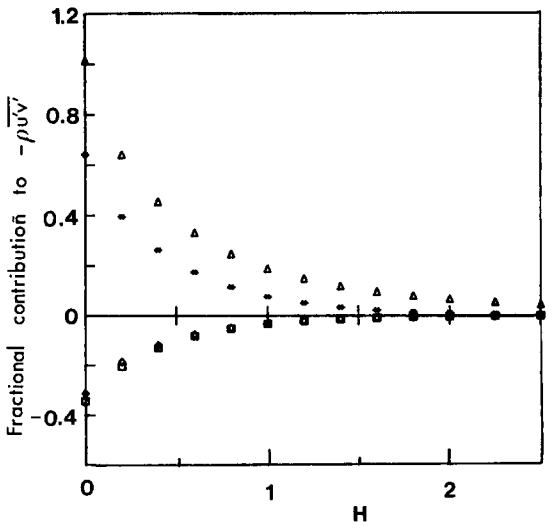

FIG. 11. Fractional contribution of each quadrant to the total Reynolds stress as a function of hole size H ($U_\infty = 9.9$ m/sec, $y_+ \sim 39$). Here □ Q1, △ Q2 (ejection), ◇ Q3, * Q4 (sweep).

Downloaded 02 Oct 2003 to 129.105.69.38. Redistribution subject to AIP license or copyright, see http://ojps.aip.org/phf/phfcr.jsp

planar boundary layer[32] and the turbulent channel flow.[12] However, the fractional contribution to the Reynolds stress appears to drop off much more rapidly with H in the cylindrical case. For instance, at $H = 2$ the contribution to the Reynolds stress in the turbulent channel flow is about 0.45 compared to about 0.1 in the present case. Since energetic uv-quadrant events are associated with a large H, this indicates that events detected in the cylindrical boundary layer are less energetic than events detected in turbulent channel flow. In addition, the relative contribution of quadrants 1 and 3 are larger in the cylindrical boundary layer. At $H = 0$ the total contribution of quadrants 1 and 3 to the Reynolds stress is about -0.4 in turbulent channel flow compared to about -0.6 in this case. Events in quadrants 1 and 3 are difficult to interpret and may be related to cross-flow structures.

The conditional averages based on the uv quadrant shown in Fig. 12 are similar to the results for turbulent channel flow.[12] First, both $\langle u \rangle$ and $\langle v \rangle$ have their extreme values at the detection time where $\langle uv \rangle$ has its extreme value. Second, the width of the $\langle v \rangle$ peak controls the width of the $\langle uv \rangle$ peak. Finally, the width of the uv peak at half of its maximum amplitude is about 3 or 4 viscous time units. The outflow angle for quadrant 2 events, estimated from Fig. 12, is about 9° at $H = 1$. This is similar to the case of turbulent channel flow where the outflow angle is 12° for $H = 4$ and 10° for $H = 2$ (estimated from Ref. 12). (The outflow angle for quadrant 2 events is expected to increase with H, since the events are more energetic at a larger H.) The similarity of the uv-quadrant events once more suggests that the mechanism for the generation of the turbulence is the same in both cases.

D. Multiple probe correlations

To investigate the correlation between velocities at different points in the boundary layer, a series of experiments was performed to measure simultaneously the velocities at three locations in the boundary layer. For these experiments U probes were positioned on the top and two sides of the

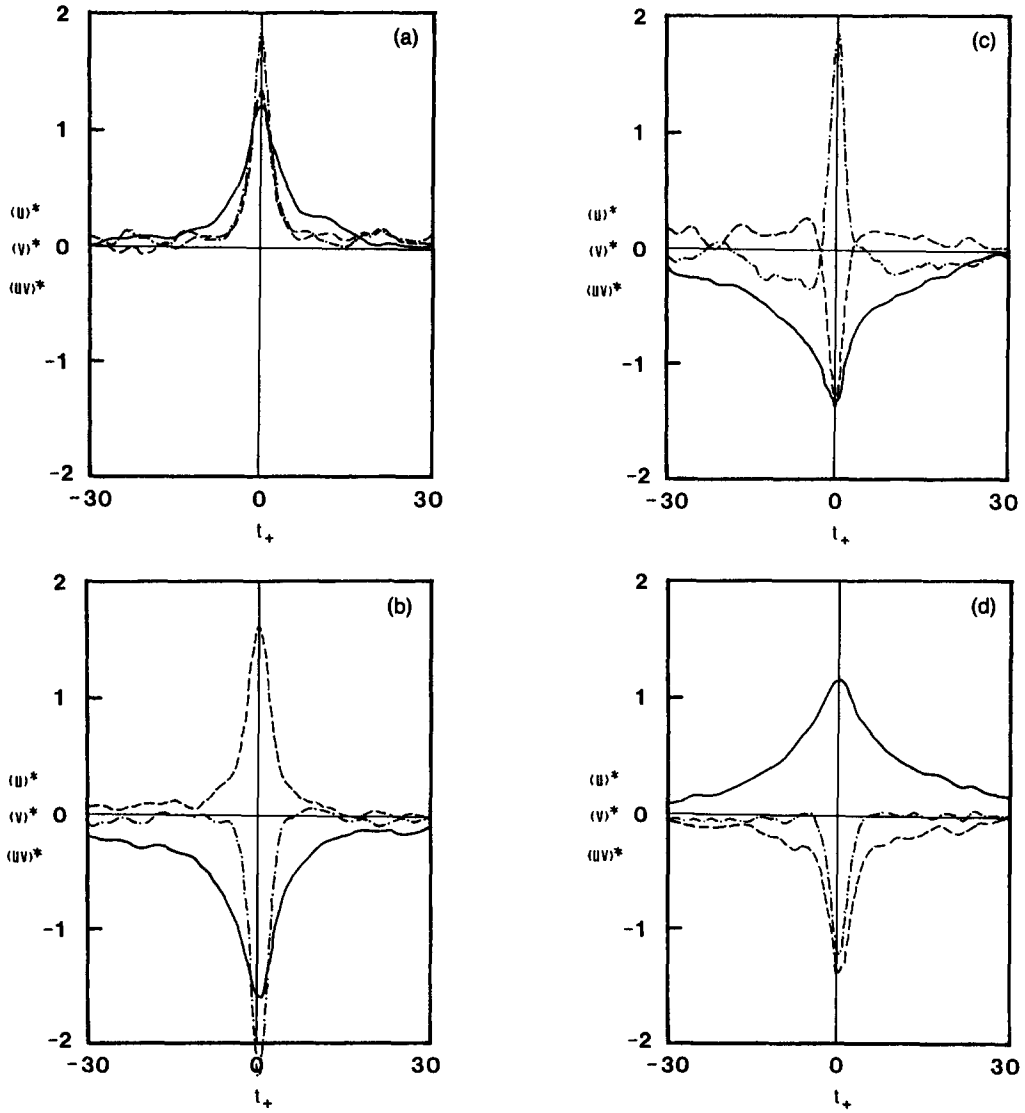

FIG. 12. Conditional averages of velocities and Reynolds stress based on uv-quadrant event detection for $H = 1$ and ($U_\infty = 9.9$ m/sec, $y_+ \sim 39$). Here — $\langle u \rangle^*$, --- $\langle v \rangle^*$, -·-·-· $\langle uv \rangle^*$. (a) Quadrant 1 events (374 members). (b) Quadrant 2 events (700 members). (c) Quadrant 3 events (420 members). (d) Quadrant 4 events (628 members).

Downloaded 02 Oct 2003 to 129.105.69.38. Redistribution subject to AIP license or copyright, see http://ojps.aip.org/phf/phfcr.jsp

cylinder, so that each probe would measure the streamwise velocity on that side of the cylinder. The top U probe had a length of $l_+ = 10$, and the two side U probes had lengths of $l_+ = 25$ at a wind tunnel velocity of 10 m/sec. Measurements were made at a location 1.4 m downstream of the trip corresponding to $Re_x \sim 10^6$. The position of the three probes is shown schematically in Fig. 13(a). All probes were positioned 0.38 cm ($y_+ \sim 115$) from the wall of the cylinder. Probe 3 was positioned a distance L upstream of probe 1, and probe 2 was at an equal distance downstream of probe 1.

The cross-correlation coefficient between the top probe 1 and the upstream probe 3, $\rho_{13}(\tau)$, where τ is the lag time, is negative as shown in Fig. 13(a). In other words, if the velocity at probe 1 is higher than the mean, then the velocity at probe 3 is lower than the mean and vice versa. Circumferentially coherent structures would result in a positive correlation. Thus, high-speed or low-speed packets of fluid do not appear to propagate as circumferentially coherent structures. The negative correlation is very surprising in light of similar experiments in the planar boundary layer. Favre, Gaviglio, and Dumas[33] found a positive correlation between U probes displaced in the spanwise direction on a flat plate. The reason for the difference between the planar boundary layer and the cylindrical boundary layer is unclear. One possible explanation is related to cross flow of structures in the cylindrical boundary layer. For instance, suppose that a high-speed sweep is moving toward the wall. When it reaches the wall, it splits with one half passing around each side of the cylinder. Each half pushes some low-speed fluid from near the wall ahead of it. Thus a probe at an azimuthal position 90° from where the sweep reaches the wall measures a low velocity. At the same time, the probe at the sweep measures a high velocity resulting in a negative cross correlation.

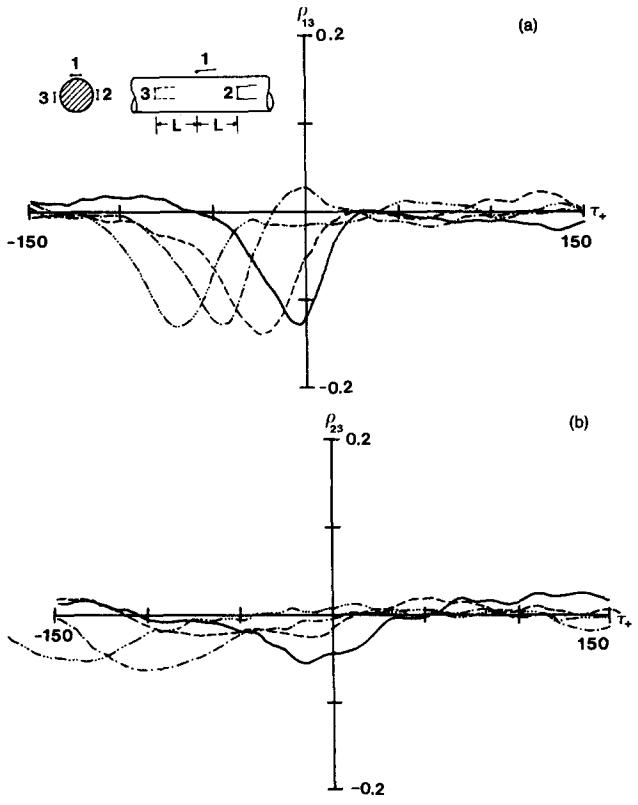

FIG. 13. Cross-correlation coefficient ρ for three U probes at different axial stations with separation L ($U_\infty = 10$ m/sec, $y_+ \sim 115$ for all probes). Here — $L/a = 0$ ($L/\delta = 0$, $L_+ = 0$), --- $L/a = 4.2$ ($L/\delta = 0.5$, $L_+ = 6.7\times10^3$), -·-·- $L/a = 8.4$ ($L/\delta = 1.1$, $L_+ = 1.3\times10^4$), ···-··· $L/a = 12.6$ ($L/\delta = 1.6$, $L_+ = 2.0\times10^4$). (a) Shows ρ_{13} (top, upstream side 3). (b) Shows ρ_{23} (downstream side 2, upstream side 3).

As the distance between probes increases, the cross-correlation minimum shifts to a more negative τ, indicating the expected phase lead of probe 3 with respect to probe 1. The advection velocity, calculated from the axial separation of the probes and τ, is nearly the same as the local mean velocity. (This calculation accounts only for the axial propagation of a turbulent structure without regard to the circumferential propagation.) Similar results appear for the cross correlation between the top probe 1 and the downstream probe 2, $\rho_{12}(\tau)$, except that the cross correlation minimum shifts to a more positive τ as the distance between the probes increases.

Probes on opposite sides of the cylinder (180° apart) have a much smaller cross-correlation magnitude than circumferentially adjacent probes (90° apart) as shown in Fig. 13(b). The advection velocity between probes 3 and 2 is estimated to be from two-thirds to one times the local mean velocity.

The magnitude of the correlation coefficient is nearly the same at different axial separations in Fig. 13, indicating that the velocity is correlated over long axial distances. In Fig. 13(b) the velocities are negatively correlated over distances of at least 13 cylinder diameters. Thus high- and low-speed lumps of fluid seem to travel in adjacent, parallel streams in the streamwise direction without any ordered swirling around the cylinder. The maximum magnitude of the correlation in this series of experiments was -0.2 for 90° adjacent probes. This is about the same magnitude as the correlation found by Favre *et al.*[33] except for the sign.

To investigate the relationship between the velocity very near the wall and the velocity further away from the wall, the top probe 1 was positioned at $y = 0.025$ cm ($y_+ \sim 8$), and probes 2 and 3 were positioned at $y = 0.25$ cm ($y_+ \sim 77$). Probe 3 was positioned upstream of probe 1, and probe 2 was positioned downstream of probe 1 as before. Figure 14 indicates that the magnitude of the cross correlation between the wall probe and the outer probe is smaller than was evident when both probes were away from the wall (Fig. 13) indicating a weaker correlation. When the axial separation of the probes is zero ($L/a = 0$), the velocity at the outer probe leads the velocity at the wall probe suggesting that a structure in the outer flow may be a precursor to a wall event. On the other hand, this may simply be a result of tilting of an eddy downstream because of differing advection velocities. By considering the cross-correlation time delay and the difference in the local mean velocities, the average angle that an eddy must be tilted is estimated to be about 50°. (To make this estimate, the effect of the circumferential offset of the probes must be neglected.) The relatively flat correlation valleys in Fig. 14(a) suggest that the relationship between structures moving toward the wall and near-wall events is somewhat weak and smeared out in time.

Downloaded 02 Oct 2003 to 129.105.69.38. Redistribution subject to AIP license or copyright, see http://ojps.aip.org/phf/phfcr.jsp

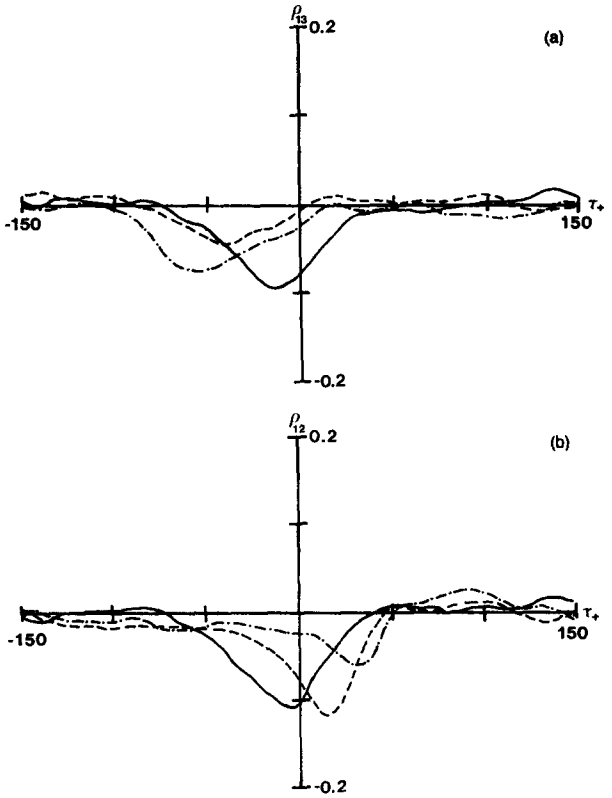

FIG. 14. Cross-correlation coefficient ρ_{ij} for three U probes at different axial stations with separation $L(U_\infty = 10$ m/sec). Top probe is at $y_+ \sim 8$ and side probes are at $y_+ \sim 77$. Here — $L/a = 0$ ($L/\delta = 0, L_+ = 0$), --- $L/a = 4.8$ ($L/\delta = 0.6$, $L_+ = 7.7\times10^3$), -·-·- $L/a = 8.4$ ($L/\delta = 1.1$, $L_+ = 1.3\times10^4$). (a) Shows ρ_{13} (top, upstream side 3). (b) Shows ρ_{12} (top, downstream side 2).

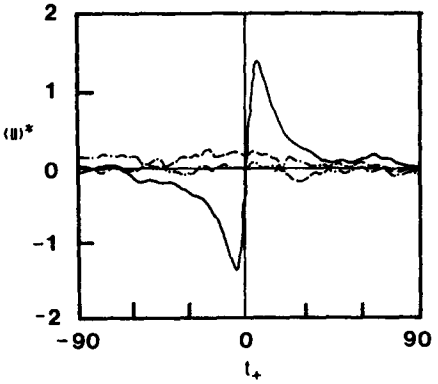

FIG. 15. The VITA detected conditional averages (154 events) for accelerating events detected at the top probe 1 using three U probes with separation $L/a = 4.8$ ($k = 1.0, T_+ = 10, U_\infty = 10$ m/sec). Top probe is at $y_+ \sim 8$ and side probes are at $y_+ \sim 77$. Here — $\langle u_1 \rangle^*$, --- $\langle u_2 \rangle^*$, -·-·-· $\langle u_3 \rangle^*$.

In Fig. 14(b) the case of near-wall structures propagating away from the wall is shown in terms of velocity cross correlations. The correlation valleys are much sharper than those in Fig. 14(a). Thus structures propagating away from the wall are more distinct than those propagating toward the wall. This is not surprising considering that typical structures moving away from the wall may be related to the ejection phase of bursts.

The lag time τ between probes is much longer in Fig. 14(a) than in Fig. 14(b) for the same axial separation. Thus outward moving events propagate at a higher velocity than inward moving events. In fact, the estimated advection velocity for outward moving events is 0.9 to 1.1 times the free-stream velocity. However, the flow disturbance of the probe mount bracket may be part of the cause of the high advection velocity. Or, if the event is dispersive in nature the advection velocity may exceed the free-stream velocity. In other words, the two probes detect a changing structure rather than the advection of an unchanging structure.

To further understand the correlation between events moving away from the wall and events moving toward the wall, event detection techniques were applied to the three U probes. A sample of the results is shown in Fig. 15 for accelerating VITA events detected at probe 1, which is closest to the wall and midway between the other probes. The downstream conditionally averaged velocity at probe 2 shows an acceleration of the fluid followed by a deceleration. This appears as a weak decelerating VITA event delayed slightly from the positive VITA event at the near-wall detection probe. Note that the negative cross correlation shown in Figs. 13 and 14 is evident from the conditional averages. The conditional average at the upstream probe 3 is nearly zero indicating that there is no upstream precursor to a VITA event at probe 1.

Similar analysis for VITA detection at the other probes also shows weak correlation between adjacent probes. Both accelerating and decelerating VITA events detected at the upstream probe 3 result in acceleration at probe 1. Events detected at downstream probe 2 have a precursor event at probe 1. In all cases there is no evidence of a relationship between events between the two most distant probes, 2 and 3. In summary, upstream events seem to be precursors to downstream events, whether or not the upstream event occurs very near the wall or a small distance from the wall. This suggests an interaction between the flow near the wall and the outer flow.

Three final notes are helpful in the interpretation of the results presented in this section. First, any correlation described in this section includes not only an axial separation and differing locations with respect to the wall, but it also includes an azimuthal separation of 90°. Second, the possibility of probe interference cannot be discounted, especially in the case of large axial separations of the probes. Third, the conditional averages have not been "aligned." It is likely that packets of fluid corresponding to events may approach a probe at different angles. Thus events detected at one probe may not be temporally aligned at a second probe, since they have propagated at slightly different angles.

V. CONCLUSIONS

Through the preceding sections of this paper, a picture of the structure of the turbulence in the boundary layer on a cylinder in axial flow has emerged. In this section the information from the earlier sections, as well as from other research, is drawn together to present a summary of the structure of this turbulent flow field.

To begin, consider the role of the wall in the cylindrical boundary layer. The wall interacts with the flow to convert

Downloaded 02 Oct 2003 to 129.105.69.38. Redistribution subject to AIP license or copyright, see http://ojps.aip.org/phf/phfcr.jsp

mean flow energy into turbulent energy that is eventually dissipated through the action of viscosity. In the planar boundary layer, the mechanism of this energy transfer is related to the burst cycle. Accelerating VITA event detection in the cylindrical boundary layer resulted in conditional averages that appear similar to those for a burst cycle in turbulent channel flow. The *uv*-quadrant event detection technique gives results for the cylindrical boundary layer that are similar to the flat plate boundary layer and turbulent channel flow in terms of conditional averages and the relative contribution of each quadrant to the total Reynolds stress. From the VITA and *uv*-quadrant event detection, it is evident that the burst mechanism for the generation of turbulence near the wall in the cylindrical boundary layer is similar to that for other wall-bounded flows. Further evidence of the similarity in the mechanism for the generation of turbulence is given by the similarity in the amplitude and distribution of the turbulence intensities between the cylindrical boundary layer and other wall-bounded flows.

Even though the mechansim for the generation of turbulence appears to be similar, some details of the burst cycle and its interaction with the outer flow seem to differ. The friction coefficient C_f is larger in the cylindrical boundary layer than in the planar boundary layer. This means that the cylindrical wall is more effective in converting mean flow energy into turbulent energy than the planar wall. It seems reasonable that this difference is related to the momentum transfer mechanism at the wall. It is possible that the spanwise vorticity, which is intensified by the sweep, may be altered by the transverse curvature of the wall. The transverse curvature may enhance the evolution of the perturbation vorticity that precedes the generation of turbulence during a burst. The result is the higher coefficient of friction measured in the cylindrical boundary layer.

Another way in which the details of the burst cycle differ between the cylindrical boundary layer and the planar boundary layer is in the interaction between the outer flow and burst events near the wall. This interaction appears to be stronger in the cylindrical boundary layer than in the planar boundary layer, as suggested by the mixed or outer scaling of the burst frequency and the relationship between the events at the wall and events away from the wall indicated in multiple probes measurements. The VITA events based on detection using multiple probes suggest that an accelerating event away from the wall may precipitate an event near the wall, and an accelerating wall VITA event detected near the wall (associated with the burst cycle) is felt downstream away from the wall very quickly.

The flow visualization results show substantial cross flow of large coherent structures in the boundary layer. Structures appear to move from one side of the cylinder to the other with little interference from the wall. It is possible that as cross-flow eddies pass near the wall moving from one side of the cylinder to the other, the flow near the wall sees the outer eddy as a sweep and reacts. Or, a sweep moving toward the cylinder may wash over the cylinder precipitating events on the sides of the cylinder.

In the cylindrical boundary layer, the ratio δ/a seems to directly control the nature of the flow. For a boundary layer transverse curvature ratio of $\delta/a \sim 1$, the largest eddies in the boundary layer are constrained by the wall just like in a planar boundary layer. As the transverse curvature ratio increases so $\delta/a > 1$, the largest eddy is less constrained by the wall, since a small deformation in the "largest eddy" allows it to pass to the opposite side of the cylinder. This effect may be related to the deviation of the coefficients of the log law for the mean velocity profile from their planar values[5] for $\delta/a > 1$. As the transverse curvature ratio δ/a gets even larger, the viscous effects associated with the wall cannot control the large-scale mixing in the boundary layer. Most of the mixing comes about from the inertia of the large eddies, and the flow is more wakelike.

Thus the assumption that the mixing length at a given point in the boundary layer is proportional to the distance from that point to the wall is not appropriate for the cylindrical boundary layer as δ/a gets large. Flow visualization confirms this. In other words, large-scale eddies are not constrained by the wall. In addition, the velocity spectra measured at varying distances from the wall are similar to one another indicating that the size distribution of eddies does not vary through the boundary layer. This supports the constant eddy viscosity closure for cylindrical boundary layers based on inertia-controlled mixing.[5,34]

ACKNOWLEDGMENTS

This research was supported jointly by the Underwater Acoustics Program, Environmental Sciences Division, and the Fluid Dynamics Program, Engineering Sciences Division, of the United States Office of Naval Research.

[1]See R. L. Richmond, AIP document no. PAPS PFLDA-28-3495-76 for 76 pages of California Institute of Technology Hypersonic Research Project Memo. No. 39 (1957). Order by PAPS number and journal reference from American Institute of Physics, Physics Auxiliary Publication Service, 335 East 45th Street, New York, NY 10017. The price is $1.50 for each microfiche (98) pages or $5.00 for photocopies up to 30 pages, and $0.15 for each additional page over 30 pages. Airmail available. Make checks payable to the American Institute of Physics.
[2]G. N. V. Rao and N. R. Keshavan, J. Appl. Mech. **39**, 25 (1972).
[3]W. W. Willmarth, R. E. Winkel, L. K. Sharma, and T. J. Bogar, J. Fluid Mech. **76**, 35 (1976).
[4]R. E. Luxton, M. K. Bull, and S. Rajagopalan, Aeronaut. J. **88**, 186 (1986).
[5]R. M. Lueptow, P. Leehey, and T. Stellinger, Phys. Fluids **28**, 3495 (1985).
[6]N. Afzal and R. Narasimha, J. Fluid Mech. **74**, 113 (1976).
[7]N. Afzal and R. Singh, Aeronaut. Q. **27**, 217 (1976).
[8]W. W. Willmarth and T. J. Bogar, Phys. Fluids **20** (10), S9 (1977).
[9]W. W. Willmarth and L. K. Sharma, J. Fluid Mech. **142**, 121 (1984).
[10]A. V. Johansson and P. H. Alfredsson, J. Fluid Mech. **137**, 409 (1983).
[11]P. S. Klebanoff, NACA Report No. 1247, 1955.
[12]P. H. Alfredsson and A. V. Johansson, J. Fluid Mech. **139**, 325 (1984).
[13]C. J. Lawn, J. Fluid Mech. **48**, 477 (1971).
[14]T. B. Hedley and J. F. Keffer, J. Fluid Mech. **64**, 625 (1974).
[15]S. Corrsin and A. L. Kistler, NACA Report No. 1244, 1955.
[16]L. S. Kovasznay, V. Kibens, and R. F. Blackwelder, J. Fluid Mech. **41**, 284 (1970).
[17]K. Fulcher, S. M. thesis, Dept. of Aeronautics and Astronautics, Massachusetts Institute of Technology, 1986.
[18]G. N. V. Rao, J. Appl. Mech. **34**, 237 (1967).
[19]V. C. Patel, A. Nakayama, and R. Damian, J. Fluid Mech. **63**, 345

Downloaded 02 Oct 2003 to 129.105.69.38. Redistribution subject to AIP license or copyright, see http://ojps.aip.org/phf/phfcr.jsp

(1974).
[20]F. M. White, *Viscous Fluid Flow* (McGraw-Hill, New York, 1974), Eqs. 6–121, p. 495.
[21]F. M. White, J. Basic Eng. **94**, 200 (1972).
[22]J. A. D. Ackroyd, J. Fluids Eng. **104**, 185 (1982).
[23]H. U. Eckert, J. Aeronaut. Sci. **19**, 23 (1952).
[24]T. Cebeci, J. Basic Eng. **92**, 545 (1970).
[25]F. M. White, R. C. Lessmann, and G. H. Christoph, AIAA J. **11**, 821 (1973).
[26]D. E. Coles, *50 Jahre Grenzschictforschung* (Vieweg, Braunschweig, 1955), p. 153.
[27]See AIP document no. PAPS PFLDA-30-2993-31 for 31 pages of NUSC Technical Report 6811 (1983) by R. M. Kennedy, H. P. Bakewell, and W. C. Zimmerman. Order by PAPS number and journal reference from American Institute of Physics, Physics Auxiliary Publication Service, 335 East 45th Street, New York, NY 10017. The price is $1.50 for each microfiche (98 pages) or $5.00 for photocopies of up to 30 pages. Airmail additional. Make checks payable to the American Institute of Physics.
[28]R. F. Blackwelder and R. E. Kaplan, J. Fluid Mech. **76**, 89 (1976).
[29]S. J. Kline, W. C. Reynolds, F. A. Schraub, and P. W. Runstadler, J. Fluid Mech. **30**, 741 (1967).
[30]R. F. Blackwelder and J. H. Haritonidis, J. Fluid Mech. **132**, 87 (1983).
[31]P. H. Alfredsson and A. V. Johansson, Phys. Fluids **27**, 1974 (1984).
[32]W. W. Willmarth and S. S. Lu, J. Fluid Mech. **55**, 65 (1972).
[33]A. J. Favre, J. J. Gaviglio, and R. J. Dumas, J. Fluid Mech. **3**, 344 (1958).
[34]R. M. Lueptow and P. Leehey, Phys. Fluids **29**, 4232 (1986).

Downloaded 02 Oct 2003 to 129.105.69.38. Redistribution subject to AIP license or copyright, see http://ojps.aip.org/phf/phfcr.jsp